

# Topological wave equation eigenmodes in continuous 2D periodic geometries

R. G. Dias,<sup>1,\*</sup> L. Madail,<sup>1,2</sup> A. Lykholt,<sup>1</sup> R. Andrade,<sup>1</sup> and A. M. Marques<sup>1,†</sup>

<sup>1</sup>*Department of Physics & i3N, University of Aveiro, 3810-193 Aveiro, Portugal*

<sup>2</sup>*International Iberian Nanotechnology Laboratory, 4715-310 Braga, Portugal*

(Dated: April 9, 2024)

In this paper, we address the topological characterization of the wave equation solutions in continuous two-dimensional (2D) periodic geometries with Neumann or Dirichlet boundary conditions. This characterization is relevant in the context of 2D vibrating membranes and our approach allows one to understand the topological behavior recently observed in acoustic three-dimensional (3D) artificial lattices. In particular, the dependence of the topological behavior on the experimental positioning of the coupling channels is explained using simple arguments and a simple method of construction of an equivalent effective tight-binding Hamiltonian is presented.

PACS numbers:

## I. INTRODUCTION

Topological quantum materials are expected to play a crucial role in next-generation quantum technologies, such as dissipationless electronics based on topological currents, protected quantum computing, and communication systems, and, not surprisingly, their study is currently among the most active fields of physics [1, 2]. It is therefore reasonable to expect that the basic formation of a Physics B.Sc. degree will soon include discussions of topological behavior in the context of condensed matter physics [3]. One may however argue that topological states of physical systems can be explained sooner in the Physics B.Sc. degree (typically, a condensed matter course is a 3rd or 4th year course taught after a quantum mechanics course).

While quantum mechanisms are intrinsic in the context of materials, topological behavior can be described by solving simple matrix equations that reflect the single-particle tight-binding description of materials. Equivalent matrix equations can be found in non-quantum mechanical systems such as acoustical lattices or coupled oscillators lattices[4–8]. In fact, the topological characterization of artificial lattices is now a hot topic of research, motivated by the fine control of effective physical parameters that allow one to probe the topological phase diagram of different models. The basic comprehension of the topological behavior of these artificial systems is within the grasp of an undergraduate physics student since it only requires knowledge of algebra and of the wave equation.

In this paper, we present a simplified approach to the topological characterization of artificial lattices by addressing the wave equation solutions in continuous 2D periodic geometries with Neumann or Dirichlet boundary conditions. This approach describes directly 2D vibrating membranes, but our focus is on its relevance to understanding the topological behavior recently observed in acoustic 3D artificial lattices. In recent papers, topological insulators (TIs) and higher-order topological insulators (HOTIs) have been generated using acoustic 3D artificial lattices, but the dependence of the topological behavior on the experimental positioning of the coupling channels, while heuristically examined [9], has not been explained as far as we know [4–6]. In this paper, we present simple arguments for the dependence of the spectra on the positioning of the coupling channels as well as a simple method of construction of an equivalent effective tight-binding Hamiltonian.

We limit our topological study to the level of a second-year undergraduate student with a physics background including a wave and vibration course and an algebra course. We do not discuss topological invariants in  $k$ -space or topological classification relying on the ten-fold table, etc., in our paper. The identification of non-trivial topological phases relies on the existence of edge/surface states and on the mapping onto effective topological tight-binding matrices. Given this simplified approach, this study could be included as a module in a computational physics course for a Physics B.Sc. degree.

The paper is organized as follows. Section II presents two simple examples of 1D TIs and a 2D weak TI and HOTI. In section III, we present a short overview of artificial lattices. Section IV discusses the wave equation and the choices of boundary conditions. In section V, we present wave equation solutions in continuous topological 2D

---

\*Electronic address: [rdias@ua.pt](mailto:rdias@ua.pt)

†Electronic address: [anselmomagalhaes@ua.pt](mailto:anselmomagalhaes@ua.pt)

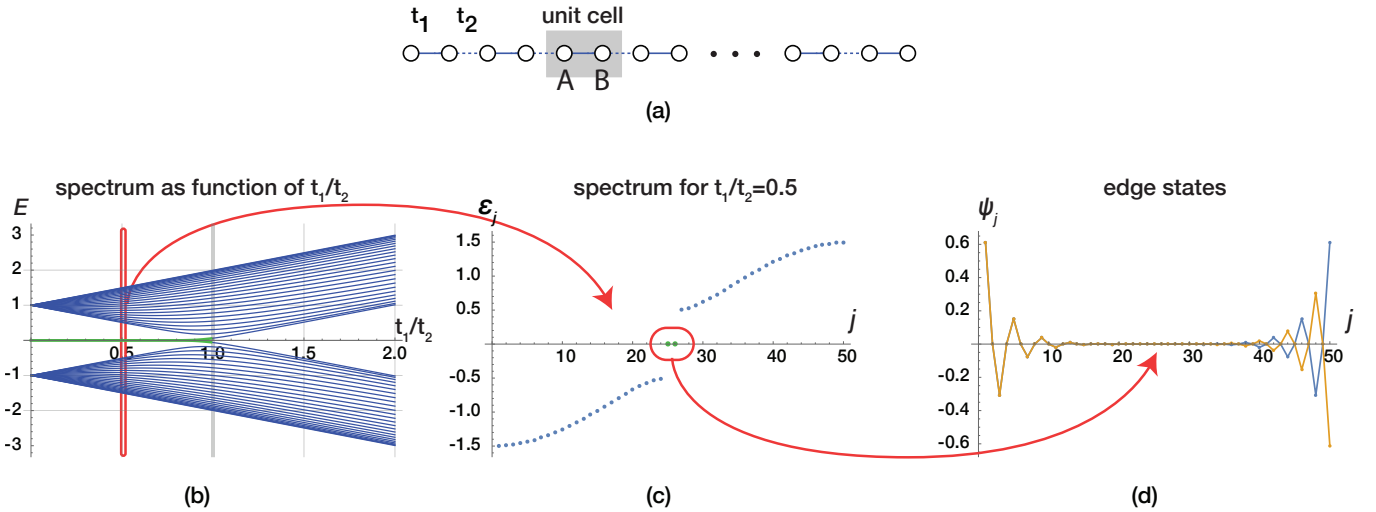


Figure 1: (a) SSH tight-binding chain with staggered hopping terms  $t_1$  and  $t_2$ . (b) Energy spectrum in units of  $t_2$  of the SSH chain with 50 sites as a function of the ratio  $t_1/t_2$ . Edge state levels are plotted in green. (c) Spectrum of the SSH chain for  $t_1/t_2 = 0.5$ . (d) Zero-energy edge states amplitudes as functions of the site index for  $t_1/t_2 = 0.5$ . Since the SSH chain is finite, the edge eigenstates are symmetric (blue curve) and anti-symmetric (orange curve) combinations of left and right edge states (with a very small energy splitting) and, therefore, are superimposed on the left side of the plot.

periodic geometries. We show in Section VI how effective tight-binding topological models can be extracted from the wave equation solutions of the previous section. Finally, we conclude in section VII.

## II. TOPOLOGICAL INSULATORS AND TIGHT BINDING MODELS

A topological insulator is usually described as an electronic material that behaves as an insulator in its interior but has protected boundary states on its edge or surface. By modifying the physical parameters of the material, these topological states may disappear, and one says the material underwent a topological phase transition from a non-trivial to a trivial phase.

This topological phase transition differs from the usual thermodynamic phase transitions in several aspects. One of them is that the usual continuous order parameter of the latter is replaced by discrete topological invariants in the former. That is, the non-trivial topological phase is signaled by discrete variations of a topological quantity. Several possible choices of topological invariants exist. All of them are equivalent, but some are simpler, while others require a deeper understanding of condensed matter theory. This manuscript adopts the simplest one: the presence of edge states with energies within the energy gaps of the system spectrum. Again, we emphasize that while one associates topological phases to quantum systems, such as electrons in crystals or cold atoms in optical lattices, topological behavior can also be found in classical systems, examples being acoustic and photonic lattices. Fundamentally, any periodic system with a band structure may display topological phases for certain parameter choices. One simple example is that of coupled oscillators forming a two-dimensional array [8]. The simplest TI is the one-dimensional Su-Schrieffer-Heeger (SSH) model [10], which is described next. The generalization of this model to two dimensions is relatively straightforward and will be addressed briefly in Subsection II.B. This generalization leads to so-called weak topological insulators that may also be higher-order TIs.

### A. SSH chain

The SSH model describes electrons hopping on a chain (one-dimensional lattice) with staggered hopping amplitudes [3], as shown in the Fig. 1(a). The chain consists of  $N$  unit cells, each unit cell hosting two sites, one on the sublattice  $A$ , and one on sublattice  $B$ .

Interactions between the electrons are neglected, and so the dynamics of each electron is described by a single-particle tight-binding Hamiltonian with a matrix representation, which is simply the adjacency matrix of the undirected lattice

graph shown in Fig. 1(a) with alternating weighted links  $t_1$  and  $t_2$ ,

$$H = \begin{pmatrix} 0 & t_1 & 0 & \dots & 0 & 0 \\ t_1 & 0 & t_2 & \dots & 0 & 0 \\ 0 & t_2 & \ddots & \ddots & \vdots & \vdots \\ \vdots & \vdots & \ddots & \ddots & t_2 & 0 \\ 0 & 0 & \dots & t_2 & 0 & t_1 \\ 0 & 0 & \dots & 0 & t_1 & 0 \end{pmatrix}. \quad (1)$$

A sequential numbering of the graph nodes is implicit in the previous tridiagonal matrix, but the physics is independent of the indexing choice. As in the case of every solid-state system, a somewhat artificial separation between bulk and boundary can be defined in the SSH chain. The bulk is the long central part of the chain, the boundaries are the two ends, or edges of the chain, indicated by shading in Fig. 1(a). The diagonalization of the previous matrix in the case of 50 sites as a function of the ratio  $t_1/t_2$  generates the spectrum shown in Fig. 1(b) with a topological phase for  $t_1/t_2 < 1$  and a trivial phase for  $t_1/t_2 > 1$ . The topological phase is signaled by the presence of two (nearly) zero energy states at the middle of the gap between the bands, as shown in Fig. 1(c). These two states are edge states with large amplitudes at the edges of the chain and exponentially vanishing amplitudes in the bulk of the chain [see Fig. 1(d)]. Due to the finite size of the chain, left and right edge states hybridize leading to eigenstates which are symmetric (blue curve) and anti-symmetric (orange curve) combinations of left and right edge states (with a very small energy splitting).

The existence of zero energy states at the middle of the gap between the SSH bands, as shown in Fig. 1(c), can be understood in the limit where the weak-link hopping parameter [ $t_1$  in the case of Fig. 1(c)] goes to zero. In this limit, the SSH chain becomes a set of uncoupled dimers (the inter-dimer hopping constant being  $t_2$ ) except for one single site at each of the edges of the chain [that is, Fig. 1(a) with only the dashed lines]. These isolated sites generate two levels of zero energy while the dimers lead to two highly degenerate levels of energies  $\pm t_2$ . In the case  $t_1/t_2 > 1$ ,  $t_2$  becomes the weak link, and if it goes to zero, only dimers are present.

Note that the spectrum in Fig. 1(b) is symmetric, that is, the positive and negative parts are mirror-like. This is a property of bipartite tight-binding lattices (i.e., lattices that can be divided into two sublattices, A and B, such that sites in sublattice A only connect to sites in sublattice B, and vice versa) and reflects the existence of the so-called chiral (sublattice) symmetry [11].

## B. Weak and higher-order topological insulators

Weak topological insulators can be considered the simplest extension of 1D topological behavior to 2D systems [12]. In a qualitative picture, these TIs are described as stacks of coupled 1D TIs that can be decoupled by applying a basis transformation. As such, these systems may exhibit edge states in a single direction,  $x$  or  $y$  (or both), with energies lying within the gap between a pair of bulk bands as in the 1D case, and one may use the 1D topological picture to describe this behavior. Higher-order topological insulators [13, 14] also exhibit boundary states, but their dimension is at least two less than that of the bulk states. In the case of a 2D higher-order topological insulator, these will be corner states.

A simple model exhibiting a simultaneous weak and higher-order topological phase is provided by the asymmetric 2D SSH model [15, 16], composed of coupled vertical and horizontal stacks of SSH chains, with non-equivalent dimerized hoppings between orthogonal directions (see Figs. 2 and 3). Again, the respective matrix representation is the adjacency matrix of the undirected lattice graph shown in Fig. 2 with alternating weighted links  $t_{1x}$ ,  $t_{2x}$ ,  $t_{1y}$ , and  $t_{2y}$ . While this adjacency matrix can be written easily just by numbering the sites, one easier alternative way is to note that the adjacency matrix for parallel SSH chains is the Kronecker product of the tridiagonal matrix of Eq. 1 with the identity matrix and the 2D SSH model can be described as the sum of the Hamiltonians of parallel SSH chains in the  $x$  and  $y$  directions (see Fig. 2). The respective eigenstates can also be written as a Kronecker product of  $x$  and  $y$  state vectors and the bulk energy dispersion relation of the 2D SSH model becomes the sum of the energy dispersion of the bands of SSH chains along  $x$  and along  $y$ , generating 4 bulk bands [see gray continua in Figs. 3(b) and (c)].

The existence of  $x$ -edge and  $y$ -edge bands in the spectrum of the 2D SSH model shown in Fig. 3(c), can be explained as in the case of the 1D SSH chain, assuming one of the hopping constants as the weakest link and considering its vanishing limit. This leads (or not) to decoupled chains at the  $x$  or  $y$  edges of the lattice, and the respective energy

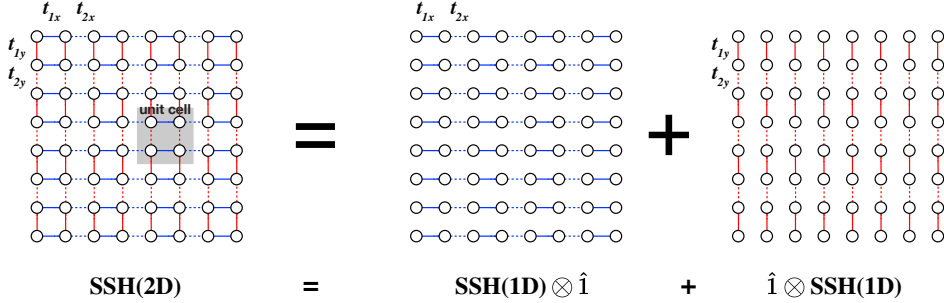


Figure 2: The 2D SSH model can be described as the sum of the Hamiltonians of two sets of parallel SSH chains in the  $x$  and  $y$  directions. The respective matrix representation is simple to find since the Hamiltonian matrix for parallel SSH chains is the Kronecker product of the tridiagonal matrix of Eq. 1 with the identity matrix. The respective eigenstates can also be written as a Kronecker product of  $x$  and  $y$  state vectors.

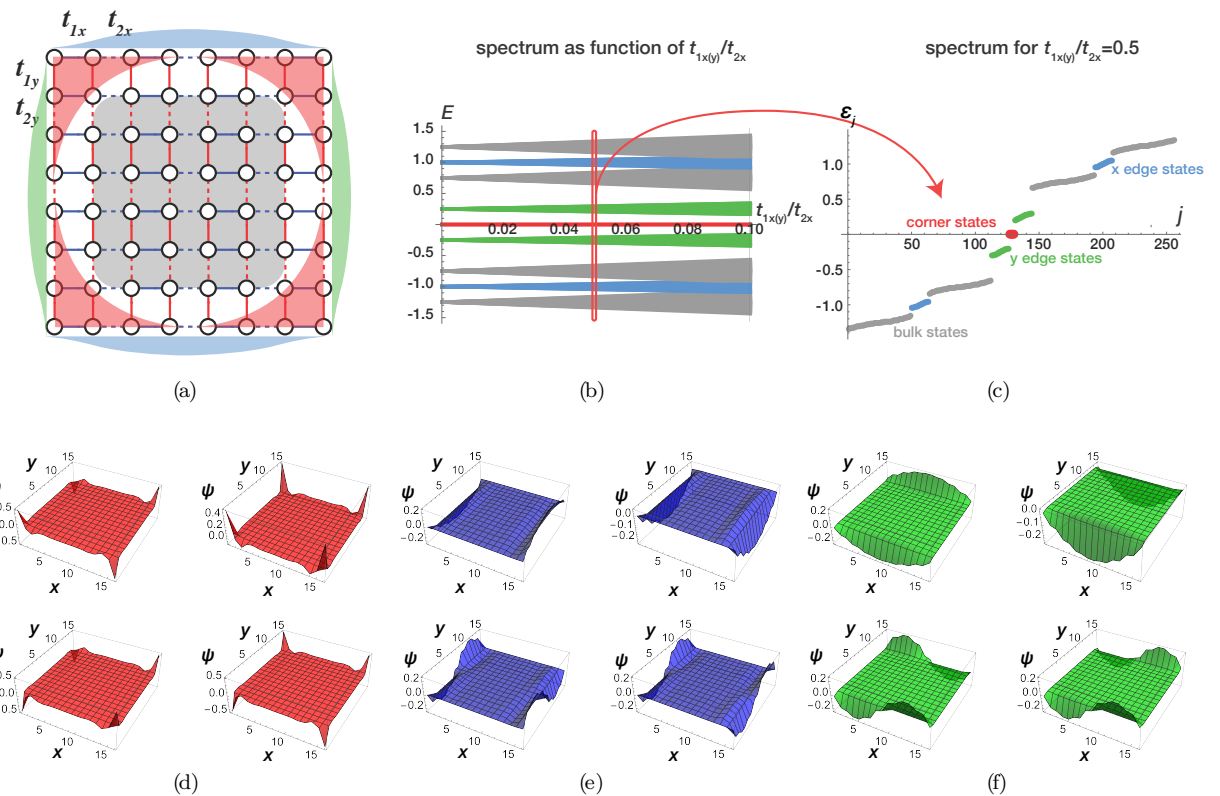


Figure 3: (a) Asymmetric 2D SSH lattice. Green (blue) shaded region indicates the localization of the horizontal (vertical) edge states, while the red shaded region indicates the localization of the corner states. (b-c) Energy spectrum for the model in (a) in the case of an open square lattice of  $8 \times 8$  unit cells, with  $t_{2x} = 1$  (the energy unit) and  $t_{2y} = 0.25$ : (b) as a function of the variation of  $t_{1x} = t_{1y}$ ; (c) for  $t_{1x} = t_{1y} = 0.5$ . (d-f) corner, horizontal edge and vertical edge states amplitudes for  $t_{1x} = t_{1y} = 0.05$ . Note that horizontal and vertical means the direction of the amplitude decay of the edge states.

levels generate two edge state bands. The corner states are found when the weak links in both the  $x$  and  $y$  directions go simultaneously to zero.

### III. ARTIFICIAL LATTICES

The first artificial lattices were constructed at the nano-scale using atomic manipulation with atomic force microscopes. The periodic positioning of atoms or molecules on a 2D substrate generated effective lattices with a chosen geometry, and particular electron wave functions would be confined to this geometry. Later, the artificial lattice

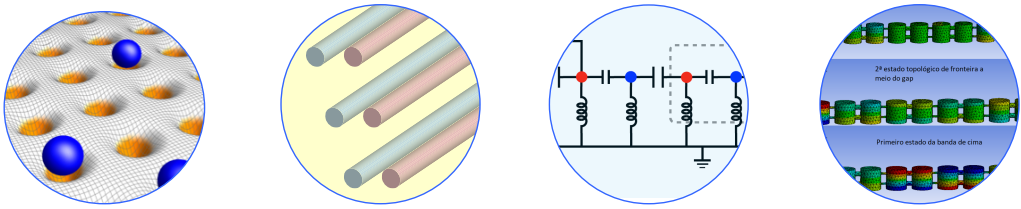


Figure 4: This figure illustrates optical, photonic, electrical circuit, and acoustic versions of artificial lattices, respectively.

concept was generalized to include optical [17], photonic [18], electrical circuit [19], acoustic [4–6], etc., networks as indicated in Fig. 4. Artificial lattice systems allow one to replicate the single-particle quantum physics of 1D, 2D, and 3D materials with the advantage of allowing the control of selected parameters of electronic systems. They also allow the introduction of local potentials, mimicking the effect of defects and impurities in crystals. Moreover, by using artificial lattices, we can validate the accuracy of models through experimental observations. One should note that tight-binding band structure calculations are simplified approaches, for example, considering only nearest-neighbor hopping terms.

In this paper, the focus is on artificial lattices that can be described by wave equation solutions of continuous 2D periodic geometries with Neumann or Dirichlet boundary conditions [20, 21]. In the case of Neumann boundary conditions, the most usual example is that of acoustic lattices. Dirichlet boundary conditions are present in the case of vibrating membranes.

#### IV. WAVE EQUATION

The wave equation is given by

$$\frac{\partial^2 u}{\partial t^2} = c^2 \Delta u, \quad (2)$$

where  $\Delta = \nabla^2 = \nabla \cdot \nabla$  is the Laplacian operator,

$$\Delta = \frac{\partial^2}{\partial x^2} + \frac{\partial^2}{\partial y^2} + \frac{\partial^2}{\partial z^2}, \quad (3)$$

$c$  is the wave velocity in the considered medium, and  $u$  can be the orthogonal displacement of a horizontal membrane from the equilibrium position or the sound pressure (difference between instantaneous pressure and static pressure) in the case of an acoustic wave [20, 21]. In 2D, the third component of the Laplacian is dropped. The resonant modes with an angular frequency  $\omega$  imply a harmonic time law of the form  $u(x, y, z, t) = e^{i\omega t} u(x, y, z)$ , which allows one to reduce the wave equation to an eigenvalue equation (Helmholtz equation),

$$-\Delta u(x, y, z) = \frac{\omega^2}{c^2} u(x, y, z). \quad (4)$$

The resonant frequencies become discrete when boundary conditions are introduced, reflecting a finite system. It is worth noting that the Helmholtz equation also arises in the Schrodinger equation for a free electron, that is, when the kinetic energy term is the only one included.

##### Wave equation for membranes: Dirichlet boundary conditions

Dirichlet boundary conditions are usually described as the absence of vibration at the boundary of the vibrating system (note that the different possible choices of the  $u$  variable for a vibrating system may imply different boundary conditions) [20, 21].

Let us consider a circular membrane of radius  $a$  initially at rest in the  $xy$  plane and centered at the origin [20, 21]. The vibration of the membrane is described by the 2D version of Eq. 2 where  $u(x, y, t)$ , is the time-dependent orthogonal

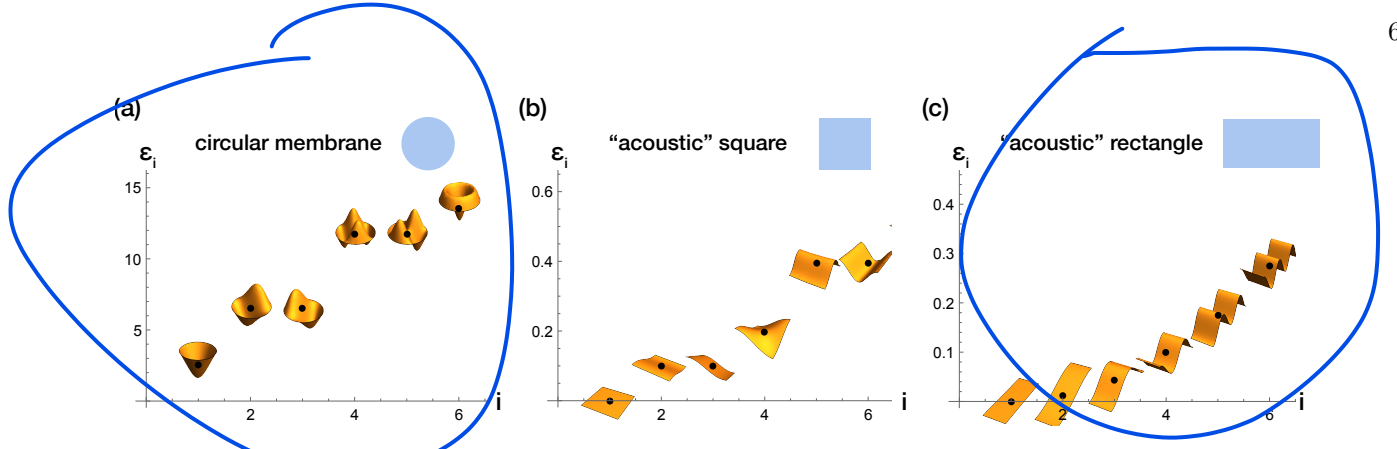


Figure 5: The six first eigenfrequencies ( $\varepsilon_i = \omega_i^2/c^2$ ) and respective eigenmodes of minus the Laplacian in the case of: (a) circular membrane of radius 1.5 with Dirichlet boundary conditions; (b) square of side 10 with Neumann boundary conditions; (c) rectangle of length 30 and width 4 with Neumann boundary conditions. Note the degeneracy in the case of the circular and square modes reflecting the  $O(2)$  symmetry of the circle and the  $C_4$  symmetry of the rectangle.

displacement of the membrane from the equilibrium position at point  $(x, y)$ . Dirichlet boundary conditions at the boundary of the membrane reflect the attachment of the membrane to a rigid frame, and therefore, we have

$$\frac{\partial^2 u}{\partial t^2} = c^2 \left( \frac{\partial^2 u}{\partial x^2} + \frac{\partial^2 u}{\partial y^2} \right), \text{ for } (x, y) \text{ within the circle}; \quad (5)$$

$$u = 0, \text{ for } |(x, y)| = a. \quad (6)$$

Adopting cylindrical coordinates,  $(r, \theta, z)$ , we can rewrite the wave equation as

$$\frac{\partial^2 u}{\partial t^2} = c^2 \left( \frac{\partial^2 u}{\partial r^2} + \frac{1}{r} \frac{\partial u}{\partial r} + \frac{1}{r^2} \frac{\partial^2 u}{\partial \theta^2} \right) \text{ for } 0 \leq r < a, 0 \leq \theta \leq 2\pi \quad (7)$$

and the method of separation of variables generates solutions of the form

$$u_{mn}(r, \theta, t) = (A \cos c\lambda_{mn}t + B \sin c\lambda_{mn}t) J_m(\lambda_{mn}r) (C \cos m\theta + D \sin m\theta), \quad (8)$$

for  $m = 0, 1, \dots$ , and  $n = 1, 2, \dots$  and where  $J_m(x)$  is the Bessel function of the first kind and order  $m$ .

The first six eigenmodes of the circular membrane with Dirichlet boundary conditions are displayed in Fig. 5(a) on top of the respective eigenfrequencies. Degeneracy is observed, reflecting rotational symmetry of the circular membrane. These modes are obtained using software that allows the numerical solution of partial differential equations. For example, using Wolfram Engine in a Jupyter Notebook frontend, these modes can be obtained with the following short script [22]:

```

boundary = Show[Graphics[Disk[{0, 0}, radius]], ImageSize -> 200];

bdr = BoundaryDiscretizeGraphics[boundary,
MaxCellMeasure -> {"Area" -> 0.01}, AccuracyGoal -> 20,
PrecisionGoal -> 20, MeshCellStyle -> {{1, All} -> Red, {0, All} -> Black}];

nmodes = 10;

{vals, funs} = NDEigensystem[{-Laplacian[u[x, y], {x, y}],
DirichletCondition[u[x, y] == 0, True]}, u[x, y],
{x, y} [Element] bdr, nmodes, Method -> {"PDEDiscretization"
-> {"FiniteElement", "MeshOptions" -> {"Area" -> 0.001}}}];

```

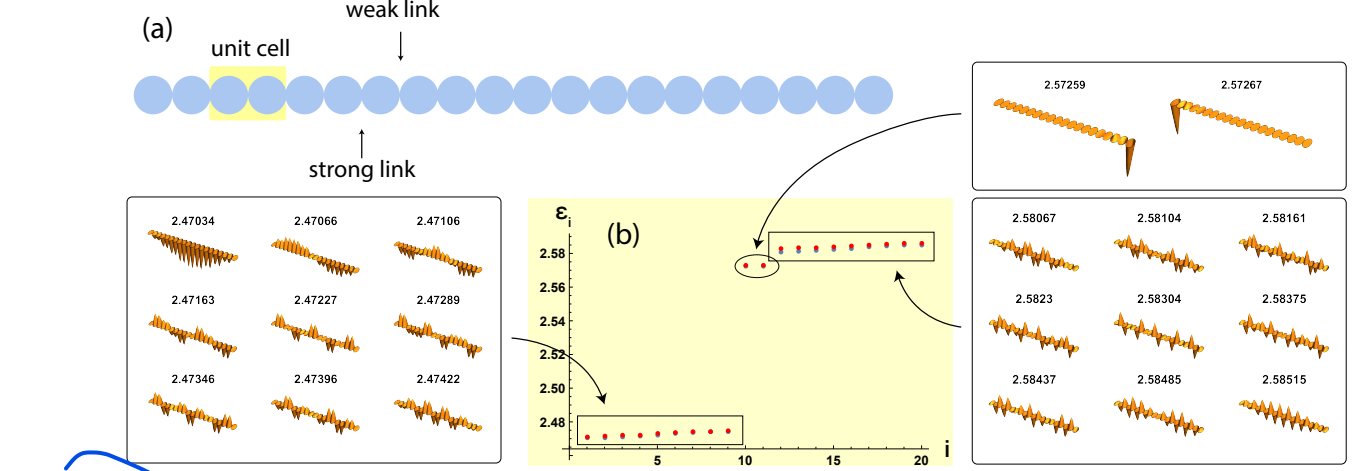


Figure 6: (a) SSH-like periodic arrangement of circular membranes with slightly different staggered separation between disk centers that imply the existence of SSH-like weak and strong links [radius equal to 1.5 and separation equal to 2.9 (strong link) and 2.99 (weak link); see Fig. 9(d) for a zoomed-in illustration of the channels between consecutive circles]. (b) First 20 eigenmodes in the case of 20 disks, with the respective eigenfrequencies (blue dots) defining two bulk bands and two edge state levels close to the top band. The red dots correspond to the eigenvalues of the respective effective tight-binding matrix as described in section VI.A, with  $t_a = 0.0017618$ ,  $t = 0.0507614$ ,  $\delta = -0.0413183$ , and  $\varepsilon_0 = 2.5741862$ .

### Wave equation for sound waves: Neumann boundary conditions

When an acoustic wave occurs in a fluid confined to the hollow space within a rigid body, the normal component of the fluid velocity vanishes at the inner surface of the body,

$$\hat{n} \cdot v = \hat{n} \cdot \nabla \phi = 0, \quad (9)$$

where  $\phi$  is the velocity potential,  $v = \nabla \phi$ . This is the Neumann boundary condition [20, 21].

Similarly, in this case, the pressure also obeys the Neumann boundary condition. This is quickly concluded by noting that the pressure and velocity potential are related by  $p = -\rho_0(\partial\phi/\partial t)$ , so that

$$\frac{\partial}{\partial t} (\hat{n} \cdot \nabla \phi) = -\frac{1}{\rho_0} \hat{n} \cdot \nabla p = 0. \quad (10)$$

An important consequence of Neumann boundary conditions is that sound waves propagate much more through small holes than waves obeying Dirichlet boundary conditions.

The previous script can also be used in case of Neumann boundary conditions, just removing the text “*Dirichlet-Condition[u[x, y] == 0, True]*”. The first six eigenmodes of an “acoustic” square and rectangle (2D regions) with Neumann boundary conditions are displayed in Fig. 5(b) and (c) on top of the respective eigenfrequencies. Degeneracy is observed in the case of the square but not in the rectangle, reflecting that  $x$  and  $y$  directions are not equivalent in the latter.

## V. WAVE EQUATION SOLUTIONS IN CONTINUOUS 2D PERIODIC GEOMETRIES

The idea behind acoustic lattices is that we may think of each of the modes described in the previous section as an atomic orbital. Therefore, effective tight-binding models are constructed with a periodic arrangement of these modes and a small coupling between them so that the single-mode description remains approximately valid in the neighborhood of each site.

In this section, we first present the eigenfrequencies and respective eigenmodes of periodic arrangements of circular membranes that show topological characteristics, namely the existence of edge states in the gap between two bands formed from the first mode of the circular membrane. In Fig. 6, we consider an SSH-like periodic arrangement of circular membranes with slightly different staggered separations between disk centers that imply the existence of SSH-like weak and strong links [see Fig. 9(d) for a zoomed illustration of the channels between consecutive circles]. The

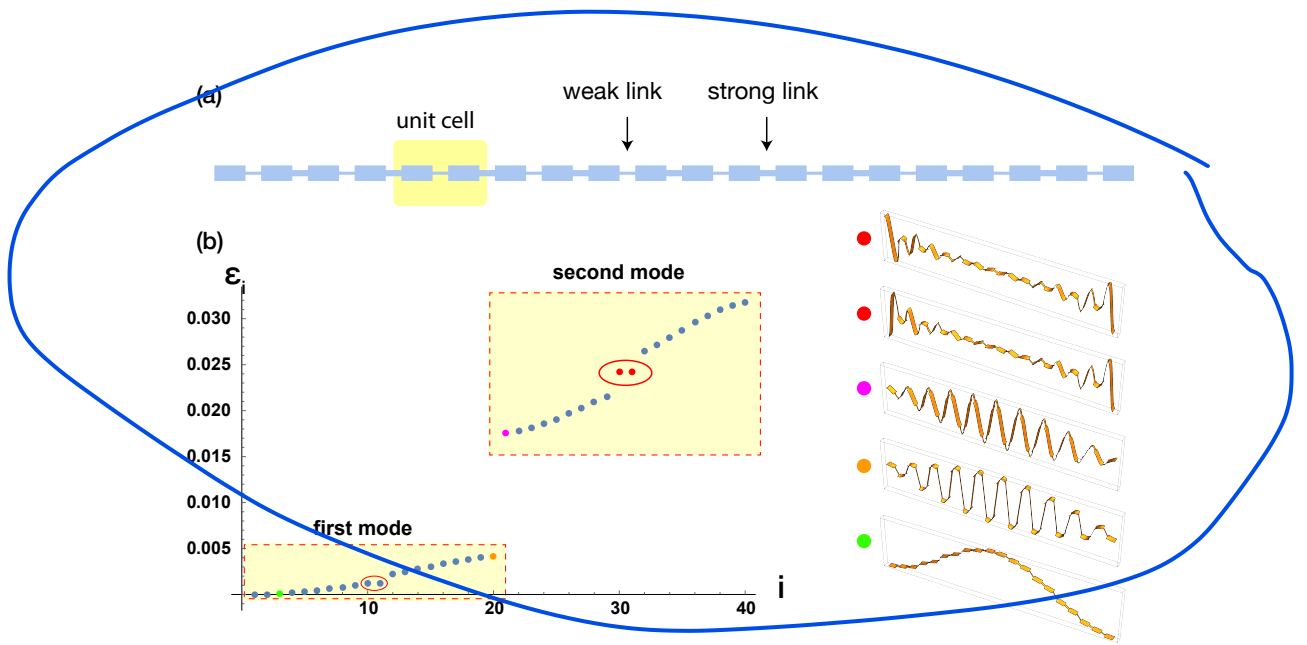


Figure 7: (a) Acoustic SSH chain of acoustic rectangles with staggered narrow and wide channels between rectangles [rectangles of width 10 and length 20; separation between rectangles centers equal to 30; channels of width equal to 2 (weak link) and 4 (strong link)]. (b) Topological bands of the rectangle chain corresponding to the first and second modes of the rectangle. On the right, examples of eigenmodes with the respective eigenfrequencies indicated by the coloring of the dots.

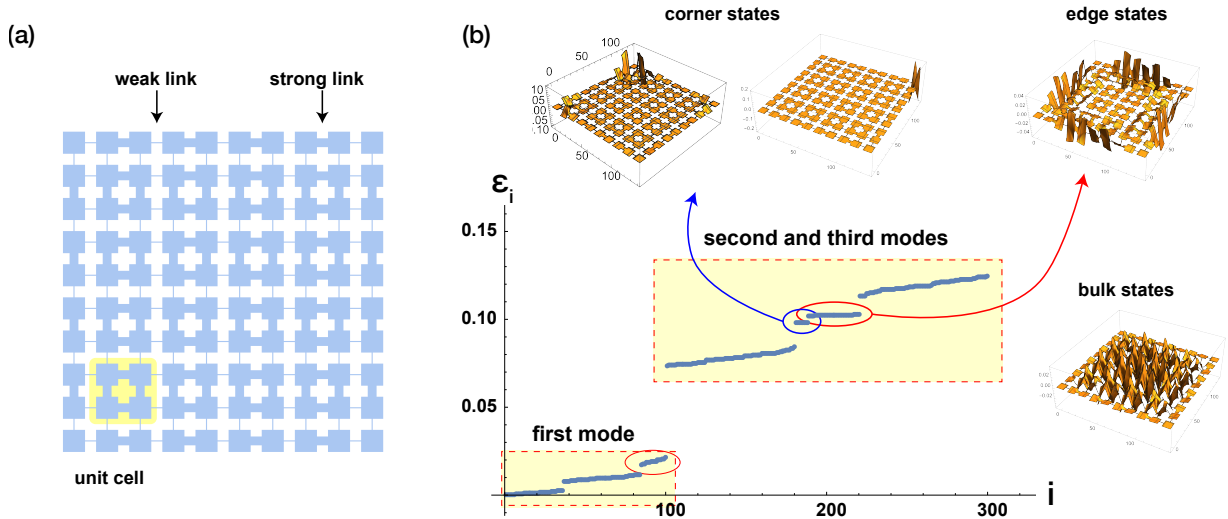


Figure 8: (a) 2D SSH geometry of coupled acoustic squares; (b) Topological bands centered at the energies of the single square first and second/third modes (see Fig. 5). Edge state levels are encircled in red and corner states in blue.

coupling of the first mode of each circle disk due to the narrow channels between disks generates resonant harmonic-like eigenmodes for the set of disks with frequencies close to that of the first mode of a single disk. However, zooming in on the spectrum it is possible to see in Fig. 6(b) that the first 20 eigenfrequencies in the case of 20 disks define two bulk bands with two edge state levels that appear close to the top band.

Note that this is not the typical SSH spectrum shown in Fig. 1, where the edge state levels appear at the gap center symmetrically distant from the top and bottom bands. In the next section, we will show how to modify the SSH tight-binding matrix to obtain an effective tight-binding description of the circular membrane chain. Ideally, an artificial lattice realization of the SSH model should exhibit edge state levels at the gap center. In the next section, we show how to achieve that in the case of an acoustic chain of rectangles by adequately choosing the coupling channels. The spectrum of such a chain is shown in Fig. 7. The sets of topological bands corresponding to the first and second

modes of the rectangle are displayed in Fig. 7(b). While edge states are present in both gaps, in the case of the second mode gap, the edge state levels are approximately at the gap center. The amplitude profiles are shown for particular modes indicated by the different colored dots. We will see that a simple argument based on the form of these profiles can be used to justify the approximately chiral (that is, symmetric) spectrum for the second mode levels.

These arguments can also be applied to 2D topological geometries, such as the one shown in Fig. 8, corresponding to a 2D acoustic version of the 2D SSH model. Edge and corner states are observed in the energy range corresponding to the second and third modes of the acoustic square. The degeneracy of the second and third modes (see Fig. 5) adds a layer of complexity; for example, the number of corner states is eight and not four, as in the case of Section II.B.

## VI. EXTRACTING EFFECTIVE HOPPING PARAMETERS

The objective of this section is two-fold: (i) to show how to obtain a tight-binding matrix that reproduces the resonant frequency spectrum of the wave equation in a 2D periodic geometry; (ii) to show how to generate a 2D geometry such that its resonant frequency spectrum replicates the spectra of a particular topological tight-binding model. In what concerns the former, the lowest number of variational hopping parameters (or local potentials) is considered that still allows to reach the objective with a good fit. The first objective is exemplified with the case of the SSH chain of circular membranes. The second is addressed replicating the SSH tight-binding model with a chain of acoustic rectangles.

### A. SSH chain of circular membranes

We have seen in the previous section that in the case of the SSH chain of circular membranes in the energy range of the first mode of the single membrane, the edge state levels appear very close to the top band [see Fig. 6(b)]. To justify the choice of a modified SSH tight-binding matrix, we first compare the eigenfrequencies of the first modes of a single membrane, a dimer, and a trimer (with a weak and a strong link) of circular membranes. These geometries and the respective eigenfrequencies are shown in Fig. 9(a). One can see that the anti-symmetric combination of the first mode in the dimer has almost the same energy (with a small positive shift) as that of the first mode of a single circular membrane, but the symmetric combination has a considerably larger negative shift. A two-site tight-binding model can correctly describe the level splitting (which is equal to the hopping parameter  $t$  between the two sites) of the bonding and anti-bonding states, but with equal symmetric shifts of the two levels. To lower the anti-bonding level, a uniform local potential  $\delta$  can be applied to the two-site tight-binding cluster,

$$\begin{pmatrix} -t & t \\ -t & t \end{pmatrix}_{\text{dimer}} = \begin{pmatrix} \varepsilon_0 + \delta & -t \\ -t & \varepsilon_0 + \delta \end{pmatrix}, \quad (11)$$

(where  $\varepsilon_0$  is the energy of the first mode of circular membrane) so that the dimer levels match the eigenvalues of the tight-binding matrix. Note that the minus sign in the off-diagonal matrix elements guarantees that the bonding state is the lowest energy state. Since the eigenfrequency of the anti-bonding mode is close to that of the single membrane [as shown in Fig. 9(a)], then  $\delta \approx -t$ . The reason why that occurs in the case of the anti-bonding mode is due to the fact that the wavefunction has to go to zero at the middle of the dimer due to the reflection symmetry and effectively, the coupling between the two circular regions is approximately zero for this state.

The simplest form of a trimer tight-binding model, shown in Fig. 9(b), can be determined from the limiting case  $t_a \ll t$  with a similar reasoning to that of the dimer above. Asking that only the bonding mode of the dimer changes its energy and only its bonding combination to the weakly linked site of the trimer changes its energy, one arrives to the matrix

$$H_{\text{trimer}} = \begin{pmatrix} \varepsilon_0 - t_a/\sqrt{2} & -t_a & 0 \\ -t_a & \varepsilon_0 - t - t_a/\sqrt{2} & -t \\ 0 & -t & \varepsilon_0 - t - t_a/\sqrt{2} \end{pmatrix}. \quad (12)$$

The  $1/\sqrt{2}$  factor in the  $t_a$  diagonal terms reflects the  $1/\sqrt{2}$  amplitude of the bonding and anti-bonding dimer states at the middle site of the trimer. This implies that the effective hopping term between the weakly linked site to the anti-bonding (or bonding) dimer state is  $t_a/\sqrt{2}$ . While this matrix describes quite well the energy levels of the trimer,

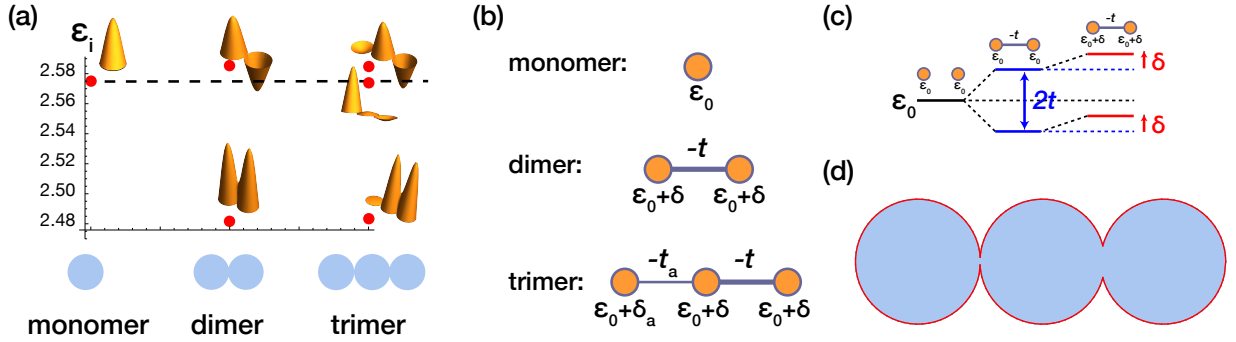


Figure 9: (a) Spectra of monomer, dimer (with a strong link) and trimer [with weak and strong links shown in (d)] of circular membranes. Radius equal to 1.5 and separation equal to 2.9 and 2.99. (b) Effective tight-binding models (which can be extracted from the energy splitting obtained when membranes are weakly connected) for the monomer, dimer, and trimer. (c) The effect of the parameters in the effective tight-binding model for the dimer. (d) Zoomed-in trimer geometry showing the narrow and wide channels between membranes.

one can obtain an exact match considering the matrix

$$H_{\text{trimer}} = \begin{pmatrix} \varepsilon_0 - t_a/\sqrt{2} & -t_a & 0 \\ -t_a & \varepsilon_0 + \delta & -t \\ 0 & -t & \varepsilon_0 + \delta \end{pmatrix}, \quad (13)$$

where now  $\delta$  is an adjustable parameter (with a value close to  $-t$ ). In this matrix, the dimer block is the dominating part and if we now consider an SSH chain of circular membranes where the weak link is considerably weaker than the strong link, this block is repeated throughout the tridiagonal matrix (for 10 membranes) in the form

$$H_{\text{SSH}} = \begin{pmatrix} \varepsilon_0 - t_a/\sqrt{2} & -t_a & 0 & 0 & 0 & 0 & 0 & 0 & 0 & 0 \\ -t_a & \varepsilon_0 + \delta & -t & 0 & 0 & 0 & 0 & 0 & 0 & 0 \\ 0 & -t & \varepsilon_0 + \delta & -t_a & 0 & 0 & 0 & 0 & 0 & 0 \\ 0 & 0 & -t_a & \varepsilon_0 + \delta & -t & 0 & 0 & 0 & 0 & 0 \\ 0 & 0 & 0 & -t & \varepsilon_0 + \delta & -t_a & 0 & 0 & 0 & 0 \\ 0 & 0 & 0 & 0 & -t_a & \varepsilon_0 + \delta & -t & 0 & 0 & 0 \\ 0 & 0 & 0 & 0 & 0 & -t & \varepsilon_0 + \delta & -t_a & 0 & 0 \\ 0 & 0 & 0 & 0 & 0 & 0 & -t & \varepsilon_0 + \delta & -t_a & 0 \\ 0 & 0 & 0 & 0 & 0 & 0 & 0 & -t_a & \varepsilon_0 - t_a/\sqrt{2} & 0 \end{pmatrix}. \quad (14)$$

Note that all membranes, except the first and the last, participate in a strong link, and their respective local potential is determined by that.

In Fig. 6(b), the energy levels obtained with this tight-binding matrix are plotted in red, and one can see a nearly perfect agreement with the eigenfrequencies (in blue) of the SSH membrane chain.

## B. SSH chain of acoustic rectangles

The spectrum of the SSH tight-binding chain has a chiral spectrum, with edge state levels equally distant from the top and bottom bands. However, edge resonant modes in vibrating systems such as the ones described in the previous sections appear shifted from the middle point between bands. This reflects the different local potential at the edge sites as shown in matrix (14). The analytical solutions to the edge perturbed system can still be found exactly [23], but go beyond the scope of this paper. The question now becomes: How do we design a geometry that corresponds to the chiral spectrum of the SSH tight-binding chain? We semi-qualitatively explain this for the case of coupled acoustic rectangles with weak and strong links.

In Fig. 10, we show trimers of acoustic rectangles with a very narrow and a very wide channel. In (a), the trimer is shorter due to a smaller separation between rectangles centers (the size of the rectangles is fixed) while in (b), the same trimer has more extended channels between rectangles due to a larger separation between rectangle centers. On the top right of (a) and (b), one can see the plots of the eigenfrequencies of the first 6 modes. The eigenfrequency of the 4th mode would determine the center energy of the lower band in the yellow region of Fig. 7 (if the dimensions

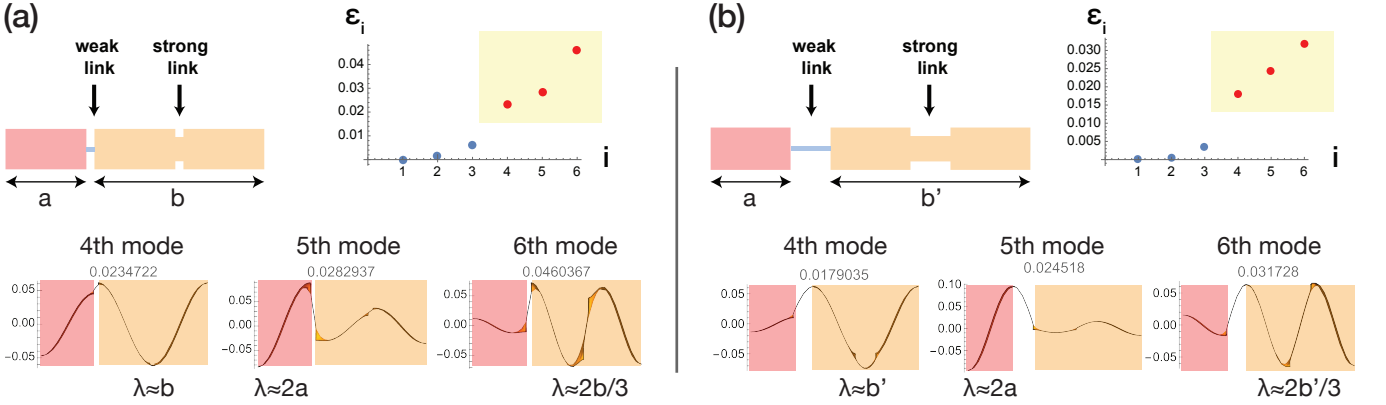


Figure 10: (a) Trimer of acoustic rectangles with a narrow and a wide channel (separation between rectangles centers equal to 22); (b) The same trimer with longer channels (separation between rectangles centers equal to 30). In both (a) and (b), rectangles of height 10 and length 20 and channels of width equal to 1 (weak link) and 6 (strong link). On the top right of (a) and (b), the plots of the eigenfrequencies of the first 6 modes are shown. We show in yellow those corresponding to the second mode of a single rectangle (4th, 5th, and 6th modes of the trimer). The side views of the respective amplitude profiles are shown at the bottom (the amplitude variation in the direction perpendicular to the trimer axis is small for these modes).

of the rectangles and channels were the same) and the eigenfrequency of the 6th mode would determine the center energy of the top band. The eigenfrequency of the 5th mode determines the position of the edge states.

We can see that in (a), the edge state frequency is not symmetrically positioned relatively to the top and bottom frequencies, but in (b) it is. The justification for this fact is implicit in the bottom figures of Fig. 10. The eigenfrequency of the 5th mode is mainly determined by the wavelength in the pink region,  $\lambda \approx 2a$ , where  $a$  is the length of the rectangles, due to the small amplitude in the orange region. This wavelength remains approximately unchanged from (a) to (b), and therefore the eigenfrequency of the edge state changes little. In the case of the 4th and 6th modes, the situation is different since their eigenfrequency is determined by the behavior in the orange region (small amplitudes in the pink region). In this region, there is a wide channel connecting two rectangles. This implies that the wavelengths of the 4th and 6th modes are determined by the length of the dimer in orange, which is given by the length of the rectangles plus that of the wide channel. Therefore, when the length of the wide channel increases, the wavelengths of the 4th and 6th modes increase, and the respective eigenfrequencies decrease, while the eigenfrequency of the 5th mode remains more or less the same. This relative shift of the 4th and 6th eigenfrequencies relatively to the 5th one translates into a shift of the SSH bands (constructed with the same parameters) in the yellow region of Fig. 7 while keeping the edge state frequencies somewhat fixed. This allows one to construct an artificial lattice that correctly reproduces the behavior of the SSH tight-binding model.

The essential point in the previous argument is that the wide channel contributes to the wavelength of the resonant modes in the dimer (formed from the second mode of the acoustic rectangle) since it is aligned with the direction of the wave vector of the resonant modes. On the other hand, the weak link plays a minor role in defining the wavelengths of the resonant modes. If we invert the ratio of the sides of the rectangles so that the rectangles are now in an upright position, keeping the channels at middle height, the lowest frequency modes of the rectangle have vertical wave vectors and the channel in the dimer does not simply add to these wavelengths. In this case, the positioning and dimensions of the channels have a complex effect on the eigenfrequency bands and edge mode frequencies. Curiously, in [9], the effect of the positioning of the channels between 3D acoustic cylinders in an SSH 1D geometry was addressed using COMSOL simulations, and the main conclusion was that the channels should be at the bottom of the cylinders in order to obtain a symmetric SSH eigenfrequency spectrum. We argue that this conclusion can be explained using our argument above, that is, the bottom coupling between cylinders allows the channels to contribute to the wavelength of the resonant modes.

We emphasize that the previous argument differs from the usual “orbital overlap” justification for the relative values of the effective hopping parameters. The uncoupled eigenmodes (that is, those in a single disk or rectangle) do not overlap when channels are introduced in the space between disks, as in the case of Figs. 7, 8, 10, and 11. In particular, in Fig. 11, we show an interesting example of the application of the argument in a 2D version of a recent acoustic lattice studied in Ref. [24]. This lattice consists of a set of short cylinders coupled by a sequence of staggered narrow and wide double channels arranged in a zigzag geometry with a  $90^\circ$  inner angle. In Fig. 11, we address the corresponding 2D version [see Fig. 11(c)], which is the top view of the acoustic lattice of Ref. [24]. The

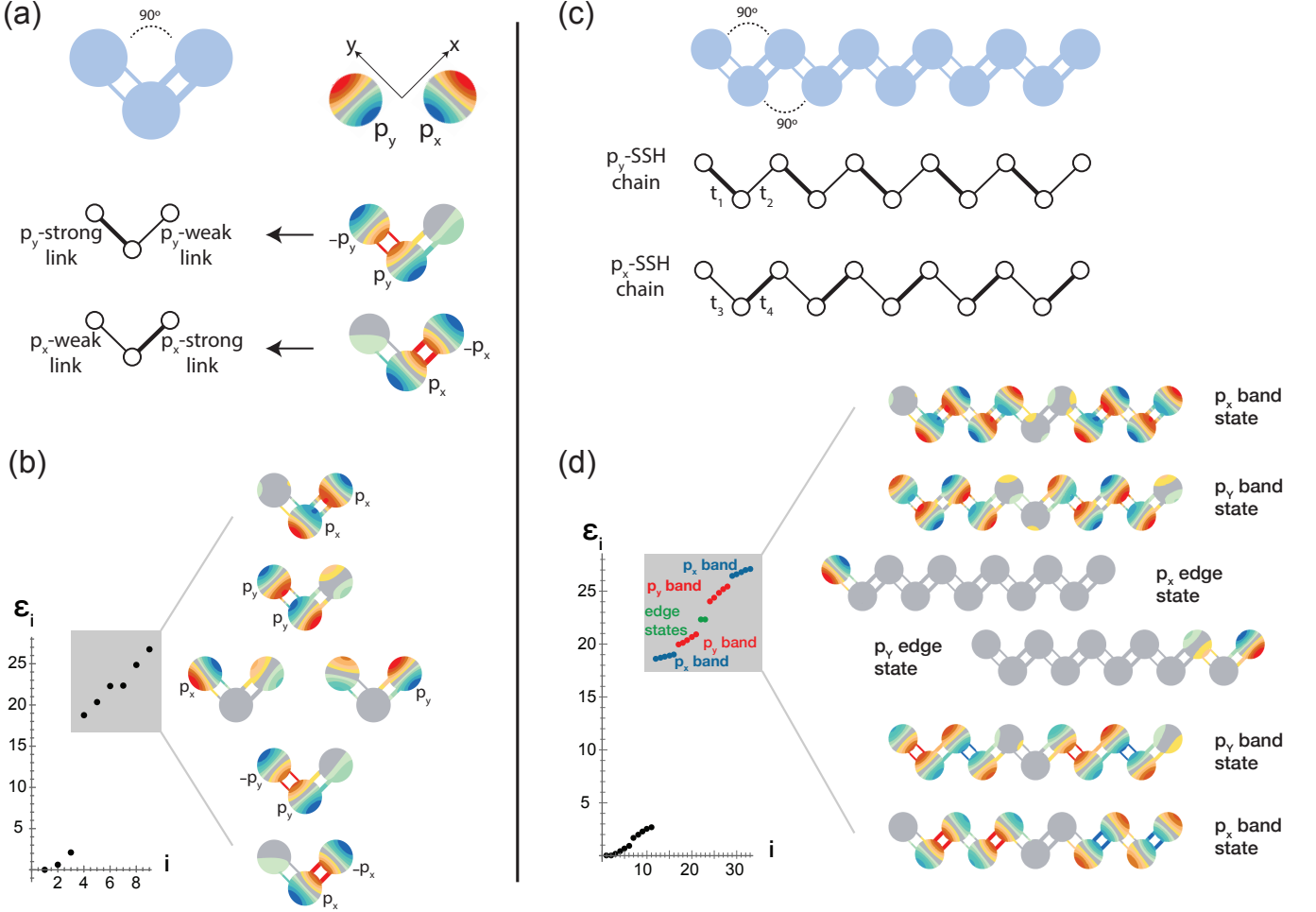


Figure 11: (a) Trimer of acoustic disks with narrow and wide double channels (disk radius equal to 0.39, separation between consecutive disk centers equal to 1, narrow channel width equal to 0.05, wide channel width equal to 0.1, channel separation equal to 0.15 and inner angle equal to  $90^\circ$ ). This trimer can be described as a set of two decoupled tight-binding trimers, a  $p_x$  trimer and a  $p_y$  trimer. (b) The respective eigenfrequency spectrum and respective eigenmodes for the frequency range overlaid in grey (corresponding to  $p_x$  and  $p_y$  eigenmodes). (c) SSH-like zigzag lattice of acoustic disks with the same channels as in (a). In the frequency range overlaid in grey in (d), the lattice can be described as a set of two decoupled SSH chains, a  $p_x$ -“orbital” SSH chain, and a  $p_y$ -“orbital” SSH chain. (d) The eigenfrequency spectrum of the SSH-like zigzag lattice of acoustic disks in (c) and examples of eigenmodes for the frequency range overlaid in grey.

second set of bands in Fig. 11(d) (grey rectangle) can be classified as  $p_x$  and  $p_y$  bands, where  $p_x$  and  $p_y$  correspond to the eigenmodes of a single disk shown in Fig. 11(a), since the respective eigenmodes show a linear combination of (approximately) only  $p_x$  or  $p_y$  modes. The same behavior is observed in a single trimer, see Fig. 11(b). This implies that in the frequency range overlaid in grey in Fig. 11(d), the lattice can be described as a set of two decoupled SSH chains, a  $p_x$ -“orbital” SSH chain and a  $p_y$ -“orbital” SSH chain, which have different hopping parameters. Interestingly, the strong and weak links change positions in the two chains, and as a consequence, a  $p_x$  left edge state and a  $p_y$  right edge state are observed in the gap between the bands.

The behavior of the SSH zigzag lattice of acoustic disks can be explained qualitatively using the previous argument in the following way. Given the orthogonal positioning of wide and narrow channels in SSH zigzag lattice, the orientation of the wide and narrow channels were chosen as the  $x$  and  $y$  directions, respectively. When examining Fig. 11(b), it becomes apparent that the lowest eigenfrequency mode in the grey region occurs when the disk orbitals are aligned with the wide channels ( $p_x$  orbitals). This alignment results in the channels increasing the wavelength the most, as reflected by the shift of the red region of the  $p_x$ -mode of the single disk to the wide double channel. The amplitudes of this mode are only large in the dimer coupled by the wide channels reflecting the much larger effective hopping term in this dimer. The above explanation for the lowest eigenfrequency mode is more or less obvious, but the second mode in the grey region is more compelling evidence of our argument. This second mode (second from the bottom

in the grey region) looks like a reflected version of the lowest mode, with  $p_y$  orbitals in the dimer coupled by the narrow double channel. This implies that for  $p_y$  orbitals, the strong link is now the one corresponding to the narrow double channel, see Fig. 11(a). This is explained by our argument, which states that the most effective position for the channels is the one that contributes more to the increase of the wavelength compared to that of the single disk modes. This positioning has a comparatively stronger effect than that of the width of the channels, leading to the exchange of weak and strong links in the case of the  $p_y$  orbitals, see Fig. 11(a).

## VII. CONCLUSION

In this paper, we have shown that the solutions of the wave equation in 2D continuous periodic geometries provide an interesting context where topological effects can be discussed. The choice of Neumann or Dirichlet boundary conditions was discussed in detail as well as their relevance to 2D vibrating membranes and acoustic artificial lattices. We have shown how to obtain simple effective tight-binding models addressing first the case of dimers and trimers. The effect of the form of the coupling channels on the relative positions of edge mode eigenfrequencies and bulk eigenfrequency bands was explained in the following way. A coupling channel in a dimer that is aligned with the direction of the wave vector of the resonant modes in each site of the dimer contributes strongly to the wavelength of the dimer resonant modes and generates a strong link in the effective tight-binding Hamiltonian of the dimer for these modes. If the channel is orthogonal to the direction of the wave vector of the resonant modes, one has a weak link.

### Acknowledgments

This work was developed within the scope of the Portuguese Institute for Nanostructures, Nanomodelling, and Nanofabrication (i3N) Projects No. UIDB/50025/2020, No. UIDP/50025/2020, and No. LA/P/0037/2020, financed by national funds through the Fundação para a Ciência e Tecnologia (FCT) and the Ministério da Educação e Ciência (MEC) of Portugal. L.M. acknowledges financial support from FCT through the grant SFRH/BD/150640/2020. A.M.M. acknowledges financial support from i3N through the work Contract No. CDL-CTTRI-46-SGRH/2022.

- 
- [1] X.-L. Qi and S.-C. Zhang, Topological insulators and superconductors, *\bibfield{journal}{\bibinfo{journal}{Rev. Mod. Phys.}}\textbf{\bibinfo{volume}{83}}, \bibinfo{pages}{1057}* (\bibinfo{year}{2011}).
  - [2] M. Z. Hasan and C. L. Kane, Colloquium: Topological insulators, *\bibfield{journal}{\bibinfo{journal}{Rev. Mod. Phys.}}\textbf{\bibinfo{volume}{82}}, \bibinfo{pages}{3045}* (\bibinfo{year}{2010}).
  - [3] J. K. Asbóth, L. Oroszlány, and A. Pályi, *A Short Course on Topological Insulators* (Springer, Berlin, 2016).
  - [4] Z. Yang, F. Gao, X. Shi, X. Lin, Z. Gao, Y. Chong, and B. Zhang, Topological acoustics, *\bibfield{journal}{\bibinfo{journal}{Phys. Rev. Lett.}}\textbf{\bibinfo{volume}{114}}, \bibinfo{pages}{114301}* (\bibinfo{year}{2015}).
  - [5] H. Xue, Y. Yang, and B. Zhang, Topological acoustics, *\bibfield{journal}{\bibinfo{journal}{Nature Reviews Materials}}\textbf{\bibinfo{volume}{7}}, \bibinfo{pages}{974}* (\bibinfo{year}{2022}).
  - [6] X. Zhang, M. Xiao, Y. Cheng, M.-H. Lu, and J. Christensen, Topological sound, *\bibfield{journal}{\bibinfo{journal}{Communications Physics}}\textbf{\bibinfo{volume}{1}}, \bibinfo{pages}{97}* (\bibinfo{year}{2018}).
  - [7] S. Huber, Topological mechanics, *\bibfield{journal}{\bibinfo{journal}{Nature Physics}}\textbf{\bibinfo{volume}{12}}, \bibinfo{pages}{621}* (\bibinfo{year}{2016}).
  - [8] R. Süsstrunk and S. D. Huber, Observation of phononic helical edge states in a mechanical topological insulator, *\bibfield{journal}{\bibinfo{journal}{Science}}\textbf{\bibinfo{volume}{349}}, \bibinfo{pages}{47}* (\bibinfo{year}{2015}), <https://www.science.org/doi/10.1126/science.aab0239>.
  - [9] S.-Y. Chen and C. Prodan, Symmetry-preserving coupling method for topological acoustic metamaterials (2023), [arXiv: 2303.06065 \[physics.app-ph\]](https://arxiv.org/abs/2303.06065).
  - [10] W. P. Su, J. R. Schrieffer, and A. J. Heeger, Solitons in polyacetylene, *\bibfield{journal}{\bibinfo{journal}{Phys. Rev. Lett.}}\textbf{\bibinfo{volume}{42}}, \bibinfo{pages}{1698}* (\bibinfo{year}{1979}).
  - [11] C.-K. Chiu, J. C. Y. Teo, A. P. Schnyder, and S. Ryu, Classification of topological quantum matter with symmetries, *\bibfield{journal}{\bibinfo{journal}{Rev. Mod. Phys.}}\textbf{\bibinfo{volume}{88}}, \bibinfo{pages}{035005}* (\bibinfo{year}{2016}).

- [12] P. Delplace, D. Ullmo, and G. Montambaux, Zak phase and the existence of edge states in graphene, \bibfield{journal}{\{\bibinfo{journal}{Phys. Rev. B}\}\textbf{\{\bibinfo{volume}\{84\}\}}, \\\bibinfo{pages}\{195452\}(\bibinfo{year}\{2011\})}.
- [13] W. A. Benalcazar, B. A. Bernevig, and T. L. Hughes, Quantized electric multipole insulators, \bibfield{journal}{\{\bibinfo{journal}{Science}\}\textbf{\{\bibinfo{volume}\{357\}\}}, \\\bibinfo{pages}\{61\}(\bibinfo{year}\{2017\}\{\nate{xlab{a}}\})}.
- [14] W. A. Benalcazar, B. A. Bernevig, and T. L. Hughes, Electric multipole moments, topological multipole moment pumping, and chiral hinge states in crystalline insulators, \bibfield{journal}{\{\bibinfo{journal}{Phys. Rev. B}\}\textbf{\{\bibinfo{volume}\{96\}\}}, \\\bibinfo{pages}\{245115\}(\bibinfo{year}\{2017\}\{\nate{xlab{b}}\})}.
- [15] G. Pelegrí, A. M. Marques, V. Ahufinger, J. Mompart, and R. G. Dias, Second-order topological corner states with ultracold atoms carrying orbital angular momentum in optical lattices, \bibfield{journal}{\{\bibinfo{journal}{Phys. Rev. B}\}\textbf{\{\bibinfo{volume}\{100\}\}}, \\\bibinfo{pages}\{205109\}(\bibinfo{year}\{2019\})}.
- [16] A. M. Marques and R. G. Dias,  $2^n$ -root weak, chern, and higher-order topological insulators, and  $2^n$ -root topological semimetals, \bibfield{journal}{\{\bibinfo{journal}{Phys. Rev. B}\}\textbf{\{\bibinfo{volume}\{104\}\}}, \\\bibinfo{pages}\{165410\}(\bibinfo{year}\{2021\})}.
- [17] F. Mei, S.-L. Zhu, Z.-M. Zhang, C. H. Oh, and N. Goldman, Simulating  $Z_2$  topological insulators with cold atoms in a one-dimensional optical lattice, \bibfield{journal}{\{\bibinfo{journal}{Phys. Rev. A}\}\textbf{\{\bibinfo{volume}\{85\}\}}, \\\bibinfo{pages}\{013638\}(\bibinfo{year}\{2012\})}.
- [18] M. Kremer, I. Petrides, E. Meyer, M. Heinrich, O. Zilberberg, and A. Szameit, A square-root topological insulator with non-quantized indices realized with photonic aharonov-bohm cages, \bibfield{journal}{\{\bibinfo{journal}{Nature Communications}\}\textbf{\{\bibinfo{volume}\{11\}\}}, \\\bibinfo{pages}\{907\}(\bibinfo{year}\{2020\})}.
- [19] V. V. Albert, L. I. Glazman, and L. Jiang, Topological properties of linear circuit lattices, \bibfield{journal}{\{\bibinfo{journal}{Phys. Rev. Lett.}\}\textbf{\{\bibinfo{volume}\{114\}\}}, \\\bibinfo{pages}\{173902\}(\bibinfo{year}\{2015\})}.
- [20] G. Arfken, G. Arfken, H. Weber, and F. Harris, *Mathematical Methods for Physicists: A Comprehensive Guide* (Elsevier Science, 2013).
- [21] N. Asmar, *Partial Differential Equations with Fourier Series and Boundary Value Problems: Third Edition*, Dover Books on Mathematics (Dover Publications, 2017).
- [22] W. Research, NDEigensystem, <https://reference.wolfram.com/language/ref/NDEigensystem.html> (2023).
- [23] A. M. Marques and R. G. Dias, Analytical solution of open crystalline linear 1d tight-binding models, \bibfield{journal}{\{\bibinfo{journal}{Journal of Physics A: Mathematical and Theoretical}\}\textbf{\{\bibinfo{volume}\{53\}\}}, \\\bibinfo{pages}\{075303\}(\bibinfo{year}\{2020\})}.
- [24] F. Gao, X. Xiang, Y.-G. Peng, X. Ni, Q.-L. Sun, S. Yves, X.-F. Zhu, and A. Alú, Orbital topological edge states and phase transitions in one-dimensional acoustic resonator chains, \bibfield{journal}{\{\bibinfo{journal}{Nature Communications}\}\textbf{\{\bibinfo{volume}\{14\}\}}, \\\bibinfo{pages}\{8162\}(\bibinfo{year}\{2023\})}.



